

See discussions, stats, and author profiles for this publication at: <https://www.researchgate.net/publication/231652223>

# Size-Dependent Stability of Supported Gold Nanostructures onto Ceria: an HRTEM Study

ARTICLE in THE JOURNAL OF PHYSICAL CHEMISTRY C · MAY 2009

Impact Factor: 4.77 · DOI: 10.1021/jp9001115

CITATIONS

22

READS

42

## 5 AUTHORS, INCLUDING:



Jérôme Majimel

French National Centre for Scientific Resea...

67 PUBLICATIONS 648 CITATIONS

SEE PROFILE



Mélanie Majimel

French National Centre for Scientific Resea...

4 PUBLICATIONS 30 CITATIONS

SEE PROFILE



Iona Moog

Johnson Matthey

4 PUBLICATIONS 25 CITATIONS

SEE PROFILE



Mona Tréguer

French National Centre for Scientific Resea...

77 PUBLICATIONS 1,415 CITATIONS

SEE PROFILE

## Size-Dependent Stability of Supported Gold Nanostructures onto Ceria: an HRTEM Study

J. Majimel,<sup>\*,†</sup> M. Lamirand-Majimel,<sup>‡</sup> I. Moog,<sup>†</sup> C. Feral-Martin,<sup>†</sup> and M. Tréguer-Delapierre<sup>†</sup>

ICMCB/CNRS, Université de Bordeaux, 87 avenue du Docteur Schweitzer, 33608 Pessac, France, and ENSCPB, 16 avenue Pey Berland, 33607 Pessac, France

Received: January 6, 2009; Revised Manuscript Received: March 23, 2009

Gold nanoparticles of various sizes, supported onto ceria, were synthesized using both deposition–precipitation and coprecipitation methods. Whatever the size, the study of the Au/CeO<sub>2</sub> interface confirms the existence of two preferential orientation relationships with a dislocation network which compensates the 25% interfacial lattice mismatch. Behaviors of supported gold nanostructures under the electron beam were examined by high-resolution transmission electron microscopy (HRTEM). The thermal stability of the gold nanostructures was found to be strongly affected by the particle size. For small nanostructures (<5 nm), reversible shrinkage of gold layer by layer onto ceria surface was observed. For larger ones, a progressive and irreversible encapsulation by a CeO<sub>2-x</sub> layer was found and a four-step process was experimentally underlined.

## 1. Introduction

Although Michael Faraday pointed out in 1834 the ability of a platinum plate to recombine hydrogen and oxygen that had been separated by the electrolysis of water, gold has been regarded for a long time as a catalytically inactive material because of its chemical inertness toward almost all elements and compounds.<sup>1,2</sup> Nevertheless, more than 30 years ago, it was shown that gold, despite its limited adsorption properties, could catalyze reactions including CO oxidation, alkene hydrogenation, and ethylene hydrochlorination.<sup>3</sup> The past two decades have seen a strong interest in gold for catalysis, owing to the seminal works of Haruta and Hutchings<sup>4–6</sup> showing that small supported gold particles (3–5 nm) can exhibit high activity in CO oxidation at low temperature. The quantum size effect observed in correspondence of the small gold particle size is essential for attaining active catalysts.<sup>7,8</sup> Consequently, several methods for the preparation of highly active support have been developed. Beyond the classical deposition–precipitation (DP) route proposed by Haruta, other methods such as coprecipitation (CP), cosputtering, chemical vapor deposition, grafting, and adsorption of gold colloids on metal oxides have been investigated.<sup>5,9–13</sup>

With the aim of improving catalytic properties, gold has been supported on various oxides such as TiO<sub>2</sub>, Al<sub>2</sub>O<sub>3</sub>, Fe<sub>2</sub>O<sub>3</sub>, CoO<sub>4</sub>, NiO, SiO<sub>2</sub>, ZrO<sub>2</sub>, or CeO<sub>2</sub>.<sup>5,14–27</sup> The role of any support is to stabilize and to disperse metal particles, but also to ensure an adequate metal–support interaction.<sup>20,28</sup> Its chemical composition and physical state can strongly influence the activity of the resulting catalyst.<sup>29,30</sup> Thus, a distinction between inert or reducible oxide supports is generally made on the basis of their ability to adsorb oxygen.<sup>30</sup> In the particular case of the CO oxidation reaction onto inert supports, the reaction proceeds through the dissociative adsorption of oxygen on the gold particles only, whereas onto reducible supports, oxygen is assumed to adsorb at the metal/support interface where it may, or may not, dissociate before reacting with the CO fixed on the gold particles.<sup>31,32</sup> Among all the reducible oxides, CeO<sub>2</sub>, or ceria, seems to be the more promising one, mainly on account

of its high oxygen storage capacity and its thermal stabilizing behavior.<sup>33</sup> Ceria has thus been used, over the past few years, as support for precious metal catalysts in a variety of applications such as the CO/NO reaction, CO and CO<sub>2</sub> hydrogenation, and low-temperature CO oxidation.<sup>34–36</sup> Although the detailed mechanisms of the above-mentioned reactions are not yet fully understood, the creation of a Ce<sup>4+</sup>/Ce<sup>3+</sup> redox couple is believed to play a major role in ceria-based catalysts processes.<sup>34,36</sup> In addition to that, the oxygen reducibility has been shown to be enhanced on the mixed oxide Au<sub>x</sub>Ce<sub>1-x</sub>O<sub>2-d</sub> system.<sup>37,38</sup>

The catalytic activity is also sensitive to the crystalline structure of the gold/metal oxide interface.<sup>30,39</sup> Previous studies underlined that gold exhibits two orientation relationships with the supporting ceria particles: (111)[ $\bar{1}10$ ]<sub>CeO<sub>2</sub></sub>//(111)[ $\bar{1}10$ ]<sub>Au</sub> and (111)[ $\bar{1}10$ ]<sub>CeO<sub>2</sub></sub>//(111)[ $\bar{1}10$ ]<sub>Au</sub>.<sup>40–44</sup> Depending on changes in the oxidation state or the density of oxygen vacancies in CeO<sub>2</sub> support, gold nanoparticles can shrink layer by layer down to Au monolayer and recover when the beam is turned off.<sup>42,44</sup> Strong ceria reduction caused by the electron beam also leads to the formation of Au–Ce alloy near or at the interface and involved the encapsulation of a gold particle by a CeO<sub>2-x</sub> layer.<sup>43</sup> This deactivation phenomenon, known as metal decoration, has already been observed for other systems, such as Pt or Rh/CeO<sub>2</sub>. It has been interpreted in terms of the occurrence of a so-called strong metal–support interaction (SMSI) effect<sup>45,46</sup> and reported and various other studies.<sup>43,44,47–52</sup>

In this work, gold particles of different sizes were deposited onto the surface of ceria nanostructured materials using both deposition–precipitation and coprecipitation routes. The crystallography and the structure of the interface between Au and CeO<sub>2</sub> were first investigated. Then the stability of the gold islands onto ceria surfaces was examined using HRTEM. The high-energy electron beam naturally induces reduction conditions<sup>53–57</sup> as well as local changes in temperature. Behaviors of the deposited gold nanostructures were shown to be strongly dependent on their size.

## 2. Experimental Procedures

**Materials. Deposition–Precipitation Method.** To produce high surface area gold-supported catalysts, cerium hydroxide was first precipitated by adding 20.16 mL of cerium(III) nitrate

\* Corresponding author. Tel.: +33 (5) 40003198. Fax: +33 (5) 40002761. E-mail: majimel@icmcb-bordeaux.cnrs.fr.

<sup>†</sup> ICMCB/CNRS.

<sup>‡</sup> ENSCPB.

solution  $\text{Ce}(\text{NO}_3)_3$  ( $[\text{CeO}_2] = 496 \text{ g/L}$ ) to 30 mL of 30% aqueous ammonia. The precipitate was stirred for 4 h at room temperature, centrifuged, and washed three times with deionized water and then air-dried at  $100^\circ\text{C}$  for 8 h. The pale-yellow solid was finally calcinated for 6 h at  $600^\circ\text{C}$ . The  $\text{CeO}_2$  nanoparticles were then dispersed in a suitable volume of deionized water and gold was deposited by adding an aqueous solution of  $\text{KAuCl}_4$  (the Au content was 2 wt % with respect to the weight of  $\text{CeO}_2$  support). The temperature of the solution was maintained at  $70^\circ\text{C}$  and the pH fixed to 8 by addition of  $\text{NH}_4\text{OH}$ . The dispersion was stirred for 3 h, centrifuged, and washed three times with  $\text{NH}_4\text{OH}$  and dried at  $100^\circ\text{C}$  for 8 h. The Au/ $\text{CeO}_2$ -DP catalyst was finally calcinated at  $300^\circ\text{C}$ .

**Coprecipitation Method.** Gold-supported catalyst Au/ $\text{CeO}_2$ -CP was prepared by adding a solution containing 11 mL of  $\text{Ce}(\text{NO}_3)_3$  ( $[\text{CeO}_2] = 496 \text{ g/L}$ ) and 196.6 mg of  $\text{KAuCl}_4$  gold salt to 200 mL of an aqueous 0.1 M NaOH (the initial pH value ( $\approx 13.5$ ) was kept constant by adding 2 M KOH to the solution). The precipitate was stirred 4 h, centrifuged, and washed twice with deionized water and then dried for 8 h at  $100^\circ\text{C}$ . The solid was finally calcinated at  $600^\circ\text{C}$  for 12 h.

**Methods.** X-ray diffraction (XRD) measurements were carried out at room temperature in Bragg–Brentano scattering geometry on a PANalytical X'PERT PRO diffractometer equipped with a X-celerator detector and using  $\text{Cu}(\text{K}\alpha_1/\text{K}\alpha_2)$  radiation ( $I_{\text{average}} = 0.154 \text{ nm}$ ).

Samples for transmission electron microscopy (TEM) were prepared by suspending the Au/ $\text{CeO}_2$  powder in alcohol by ultrasonication and depositing a drop of the suspension on a copper grid covered with a carbon film. The grid was finally air-dried for 15 min. TEM and high resolution TEM (HRTEM) observations were performed using a JEOL 2200 FS equipped with a field emission gun, operating at 200 kV and with a point resolution of 0.23 nm. High-resolution transmission electron microscopy micrographs and videos were acquired with a Gatan Ultrascan CCD  $2\text{k} \times 2\text{k}$  and digital diffractograms were calculated using the Gatan Digital Micrograph program. Moreover, in order to be representative and statistically meaningful, many images from several regions of various samples were recorded and the most characteristic results are presented here.

### 3. Results and Discussion

#### Structural Characteristics of Supported Au<sub>n</sub> onto CeO<sub>2</sub>

The as prepared polyhedral  $\text{CeO}_2$  support nanoparticles are monocrystalline and present an average size of about 25–30 nm. They exhibit low index  $\{111\}$  and  $\{001\}$  facets according to atomistic models.<sup>58</sup>

To investigate the structure of the obtained gold-supported catalysts,  $\text{CeO}_2$  samples as well as Au/ $\text{CeO}_2$ -CP and Au/ $\text{CeO}_2$ -DP samples were subjected to powder X-ray diffraction (Figure 1a) as well as transmission electronic microscopy. All samples display the cubic fluorite  $\text{CeO}_2$  structure. However, only Au/ $\text{CeO}_2$ -CP sample exhibits the  $(111)_{\text{Au}}$  peak from bulk gold FCC structure. TEM experiments revealed that gold islands are deposited almost uniformly on both Au/ $\text{CeO}_2$ -CP and Au/ $\text{CeO}_2$ -DP samples (Figure 1b). In both cases, gold crystallites are mainly found on the support material and not unsupported. However, their sizes are different for both samples. For the Au/ $\text{CeO}_2$ -DP, deposited gold particle sizes remain below 5 nm. For the Au/ $\text{CeO}_2$ -CP, a relatively wide crystallite size distribution, between 3 and 20 nm, is found due to pH variations during gold deposition. One attributes the detection of the  $(111)_{\text{Au}}$  peak on the Au/ $\text{CeO}_2$ -CP XRD pattern to the presence of larger gold islands ( $>5 \text{ nm}$ ).

Typical HRTEM images of the Au/ $\text{CeO}_2$  interface of samples prepared by both methods are visible in Figures 2, b and d. They sit at the metal–oxide interface. One can recognize the well-established dodecahedral shape of the particle when formed on ceria support. Figure 2 shows HRTEM images where the incident electron beam is parallel to the  $[\bar{1}10]$  and  $[1\bar{1}0]$  zone axis of the gold structure, respectively. Gold nanoparticles are exclusively deposited on the lower energy  $\{111\}_{\text{CeO}_2}$  surfaces<sup>59</sup> and two orientation relationships between the gold islands and the ceria support particles coexist and can be determined as  $(111)[\bar{1}10]_{\text{CeO}_2}/(111)[\bar{1}10]_{\text{Au}}$  (A-type) and  $(111)[\bar{1}10]_{\text{CeO}_2}/(111)[1\bar{1}0]_{\text{Au}}$  (B-Type). These orientation relationships are in good agreement with those already observed for the Au/ $\text{CeO}_2$  catalysts and more generally speaking for noble-metal/ $\text{CeO}_2$  materials.<sup>40–44</sup> The reticular planes facing each other from both sides of the interface plane can be  $\{111\}_{\text{Au}}$  and  $\{111\}_{\text{CeO}_2}$  or  $\{111\}_{\text{Au}}$  and  $\{002\}_{\text{CeO}_2}$  as represented in Figure 3. The lattice spacings are 0.235, 0.312, and 0.271 nm for  $\{111\}_{\text{Au}}$ ,  $\{111\}_{\text{CeO}_2}$ , and  $\{002\}_{\text{CeO}_2}$ , respectively. The lattice misfit is thus about 25%. It is too large to be matched elastically (Figure 3). As a consequence, a dislocation network is created in the gold phase for compensation. It is represented by the additional reticular half-planes shown in the insets of Figures 2, b and d for both samples. A dislocation can be seen every four lattice planes. It is in good agreement with the evaluated lattice misfit value of 25%. Similar dislocation network was already observed for another gold-based system,  $\text{Au}_2\text{S}/\text{Au}$ .<sup>60</sup> Note that the Au/ $\text{CeO}_2$  system could have favored a lower  $\Delta a/a$  misfit value obtained for example with a  $(002)[1\bar{1}0]_{\text{CeO}_2}/(002)[200]_{\text{Au}}$  orientation relationship with  $(220)_{\text{CeO}_2}$  and  $(020)_{\text{Au}}$  planes perpendicular to the interface plane ( $\Delta a/a \approx 6.6\%$ ). Nevertheless, the crystallographic nature of the interface planes seems to be a key point of such a gold/ceria interaction.

These observations are comparable to those obtained by recent theoretical calculations performed on the Pd/MgO system. It was shown that the lattice mismatch between the substrate and the supported metal induces tetragonal distortion in the small clusters, with a dilatation in the interface plane and a contraction in the direction perpendicular to the interface.<sup>61</sup> However, when the supported metal nanoparticle's size increases, the energy gain due to the interface adhesion is no longer sufficient to compensate for the strain due to the lattice misfit. Rows of metal atoms could then leave their preferential adsorption sites and an interface misfit dislocation is created. For larger metal nanoparticles, the dislocation could rearrange and form a periodic network.

**Stability of Gold Particles onto Ceria under Electron Irradiation.** The response of the gold supported particles to a focused electron beam excitation was examined in situ by HRTEM. The series of HRTEM images and videos recorded for the same specimen region as the electron beam was focused continuously, showing the evolution process of gold particles on ceria support prepared by DP and CP, are presented in Figures 4 and 5 respectively. The entire video sequences are available at <http://www.promethee.cnrs.fr/spip.php?article154>.

**Small-Sized Gold Islands (<5 nm).** For Au/ $\text{CeO}_2$ -DP, as early mentioned, the as-deposited gold nanoparticle (Figure 4 a) initially exhibit the typical dodecahedral morphology with identified  $\{111\}$  and  $\{002\}$  facets. The interface length with the ceria support particle is smaller than 5 nm, underlining a weak adhesion energy between gold and ceria.<sup>62</sup> Note that the orientation relationship is of A-type.

We progressively focus the electron beam on the gold/ceria interface region increasing significantly the induced irradiation

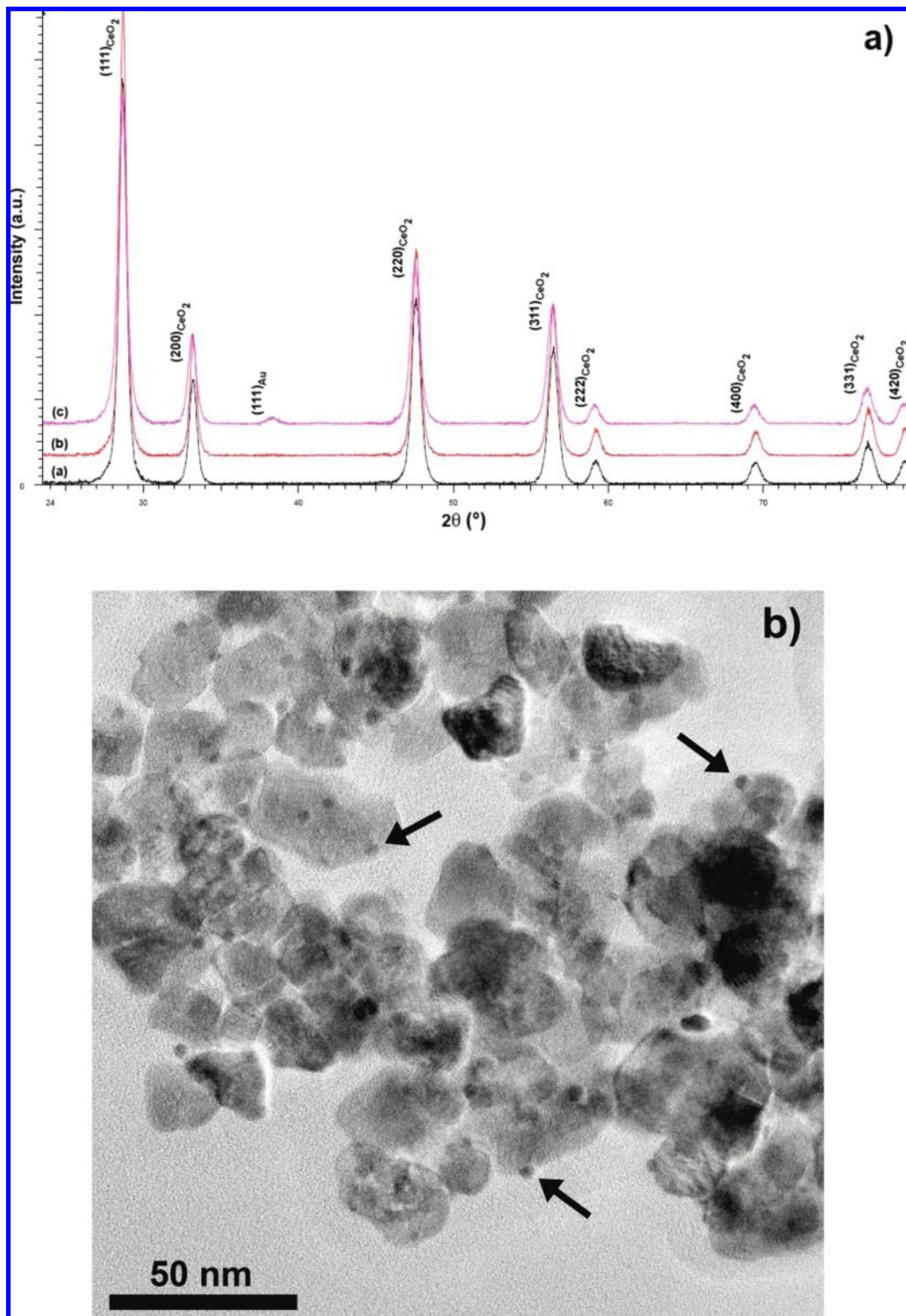


**Figure 1.** (a) XRD diffraction patterns and  $(hkl)$  reflection indexation for  $\text{CeO}_2$  support nanoparticles (a),  $\text{Au/CeO}_2\text{-DP}$  (b), and  $\text{Au/CeO}_2\text{-CP}$  (c) samples. (b) TEM micrograph of  $\text{Au/CeO}_2\text{-DP}$  sample. Dark contrasted zones correspond to homogeneously deposited gold islands (marked by arrows).

damage. In a few seconds, the morphology of the island changes and the upper left and bottom right  $\{111\}$  steps disappear (Figure 4b). The gold nanoparticle shrinks layer by layer. In a few minutes, only a gold disordered monolayer remains on the  $\{111\}_{\text{CeO}_2}$  surface but without significant change of the interface length value (Figure 4c). No other gold island or Moiré fringes could be observed on the  $\text{CeO}_2$  particle and only a slight contrast modification of the  $\{002\}_{\text{CeO}_2}$  facet could be noticed. Most of

the gold atoms may form a thin layer on the surface of the ceria particle but too thin to be detected or may have migrated out of the observed area. Moreover, it should be pointed out that, at the beginning of the electron beam exposure, there was no other gold island on the ceria substrate that could have favored either the Ostwald ripening process or the Volmer–Weber one. Even if no morphological or structural changes of the  $\text{CeO}_2$



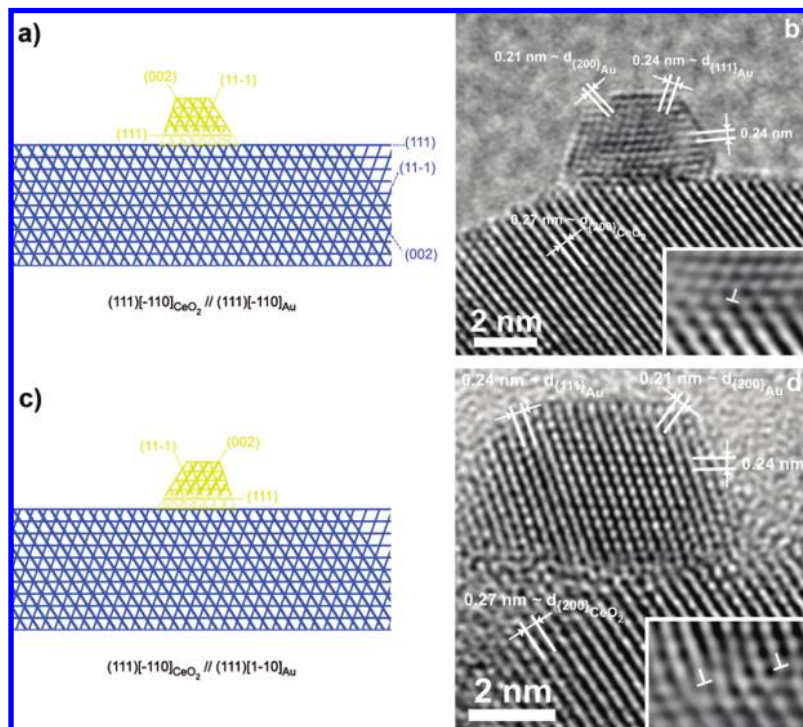


**Figure 2.** (a,c) Schematic illustrations of the two observed orientation relationships between ceria nanoparticles and gold supported islands. (b,d) HRTEM micrographs of gold islands deposited on CeO<sub>2</sub> nanoparticles following the deposition–precipitation and coprecipitation methods respectively. Dislocation networks are highlighted in the insets.

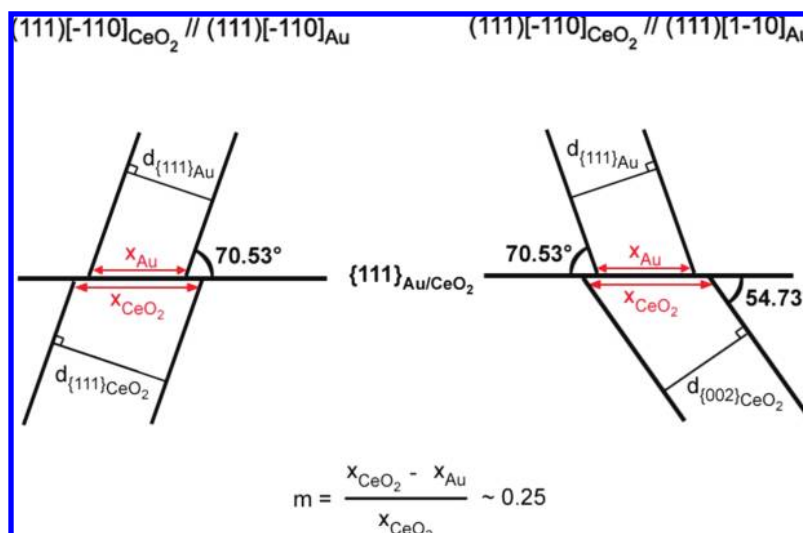


**Figure 3.** Lattice mismatch calculation for the two observed orientation relationships.

particle took place, it can be presumed that the ceria surface has been reduced by the electron beam.<sup>42</sup>

We now spread the electron beam. We observe that the gold atoms are coming back to their initial position. The thickness of the gold island gradually increases and, as soon as a structural order has been detected, the orientation relationship is identified. It is now interestingly of B-type (Figure 4d). As long as the electron beam is spread, the gold island keeps growing and the height to width ratio value becomes smaller than the initial stage one: the adhesion energy between gold and ceria increases. At the final observation stage, the height of the island is limited to 5 atomic monolayers and one can observe another dislocation network in the gold island to match the lattice misfit at the interface (Figure 4e).

The disappearance and reappearance of the gold island is entirely reversible. Additional cycles of focusing and spreading

of electron beam leads to similar atomic gold diffusion on the ceria surface.

The shrinkage process observed under focused electron beam is the result of the release of gold atoms from small nanosized particles followed by their diffusion on the substrate surface. The process mainly results from local heating phenomenon as well as creation of oxygen defects on ceria. Such dynamic processes have previously been observed by Akita et al.<sup>42–44</sup> Small nanosized gold particles have a lower melting temperature than the bulk material: particles of about 2 nm diameter have a melting temperature below 573 K.<sup>63</sup> A temperature close to the melting temperature of the small nanoparticles could typically be reached under ultrahigh vacuum conditions with a sufficient focused TEM electron beam.<sup>64</sup> Partial surface melting then becomes possible and induces the surface diffusion of atomic gold. In parallel, the oxygen vacancies are expected to be

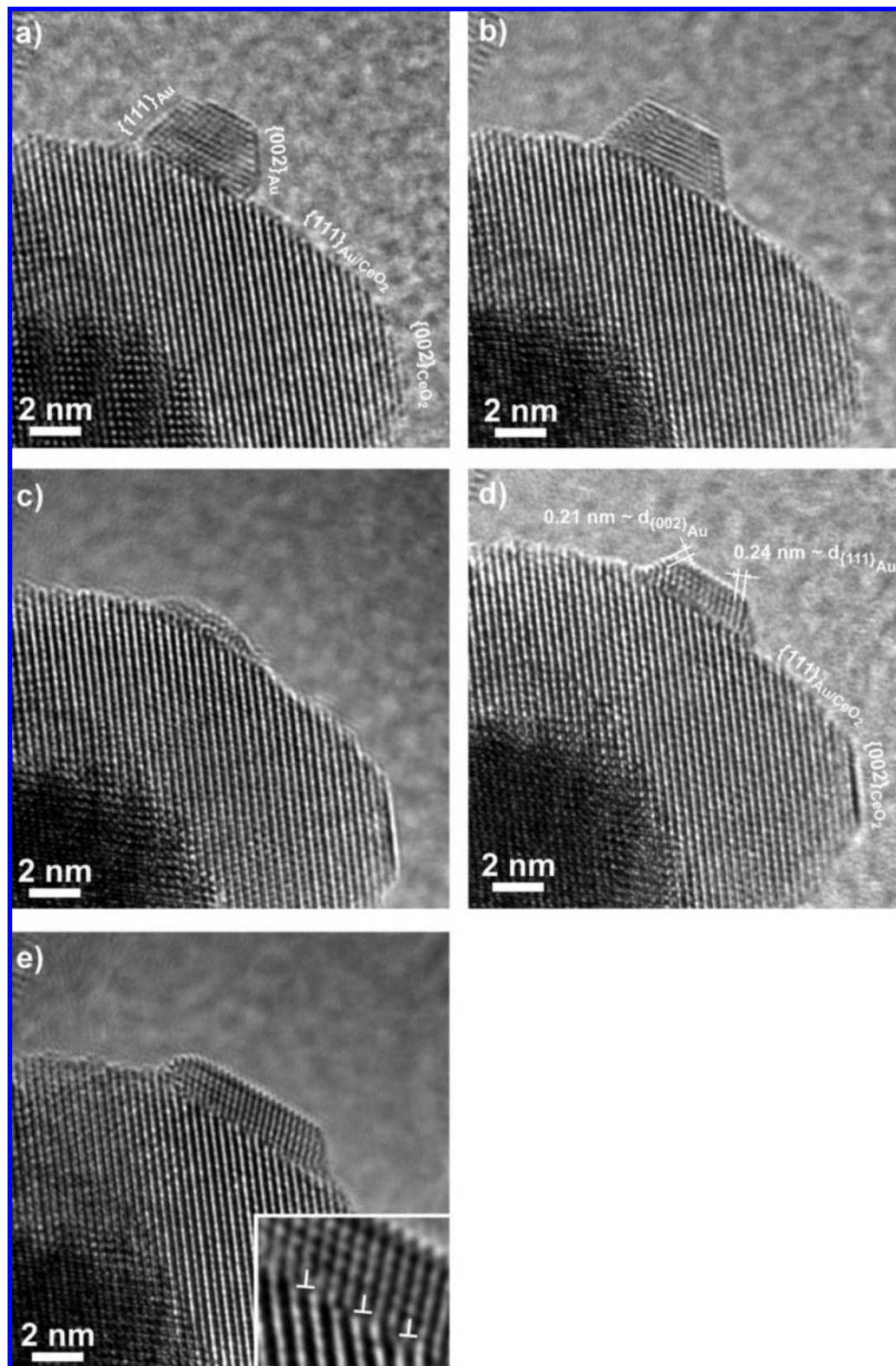


**Figure 4.** Series of HRTEM micrographs showing the diffusion process of gold atoms onto ceria surfaces and the gold island disappearance–reappearance phenomenon. (a) As-deposited gold island with A-type orientation relationship (the dislocation network is also represented in Figure 1b). (b,c) Disappearance of the gold island when the electron beam is focused on the Au/CeO<sub>2</sub> interface zone. (d,e) Reappearance of the gold island when the electron beam is spread enough to avoid irradiation damage. One can note in panel (d) the B-type orientation relationship. The dislocation network is shown in the inset of the endless stage micrograph (e).

induced by the electron beam irradiation on the substrate. The oxygen vacancies lower the activation energy barrier and act as a driving force for diffusion of gold atoms. Both processes promote the observed diffusion of the atomic gold on the

substrate surface and modify the energies of adhesion (Au–CeO<sub>2</sub>) and of cohesion (Au–Au).

More interesting is the reappearance of the gold island to its initial position under the spread electron beam. It can be



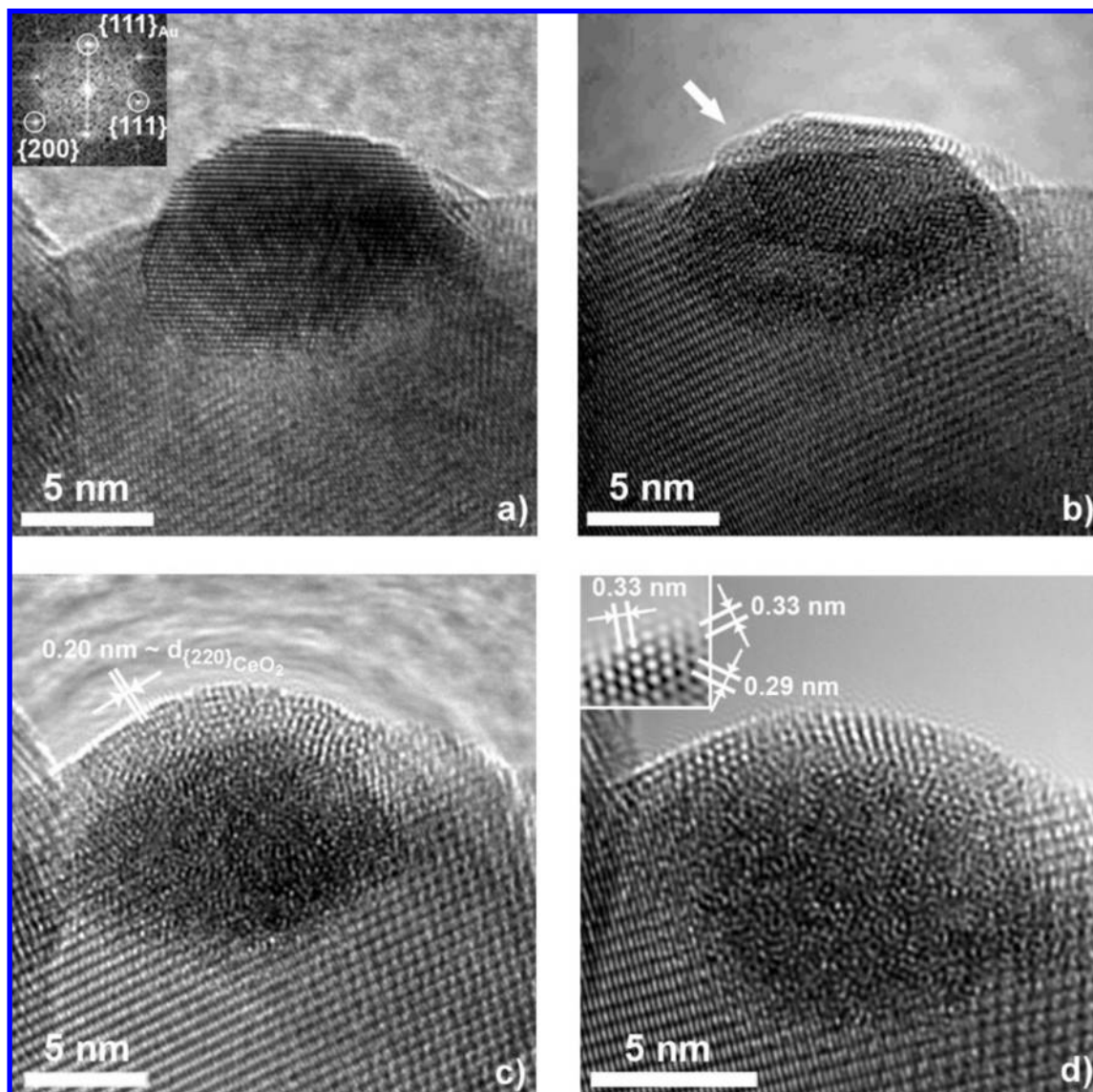


**Figure 5.** Series of HRTEM micrographs showing the encapsulation process of a gold island by a  $\text{CeO}_{2-x}$  layer. (a) As-deposited gold island and its digital diffractogram. (b) Beginning of the encapsulation of the gold nanoparticle by a thin layer (marked by arrow)—end of the video sequence. (c) Encapsulation of the gold nanoparticle by a  $\text{CeO}_2$  layer. (d) Encapsulation of the gold nanoparticle at the end of the exposure to the electron beam by a  $\text{CeO}_{2-x}$  layer. Filtered image of the encapsulating layer zone is presented in the inset.

presumed that, at the end of the focused beam exposure time, disordered gold atoms remain on the  $\{111\}_{\text{CeO}_2}$  facet. The small remaining cluster (Figure 4c) constitutes the preferred nucleation site due to its high energy state, its large surface tension, and the stronger binding energy of Au–Au bond than Au– $\text{CeO}_2$  one: the atomic gold atoms mainly diffuse and concentrate on these clusters. However, without any 3D information it cannot be assessed that all gold atoms from the first island take part in the formation of the second island. The slight observed contrast variation of the  $\{002\}_{\text{CeO}_2}$  facet might be explained by a thin gold monolayer decoration (Figures 4, c and d).

Another interesting feature is the increase of the interface length between gold and ceria from 4.5 to  $7.3 \pm 0.2$  nm. Akita et al. did not notice such a height to width ratio value decrease.<sup>42</sup> Nonetheless, after each observation, they turned off the electron beam and the sample was left in ultrahigh vacuum conditions 5–10 min before the beam was turned on again. The ceria particle could recover and neither surface reduction nor oxygen vacancies could appear.<sup>43</sup> In our experimental conditions, the creation of oxygen defects in the ceria support is favored. As a

consequence, an increase of the adhesion energy between gold and ceria is expected as predicted by theoretical calculations.<sup>61,65</sup>

Finally, particularly remarkable is the change of orientation relationship from A to B-type during the reappearance of the gold island. This structural modification is not achieved to decrease the interface lattice misfit since both A- and B-type orientation relationships induce 25% mismatch. Besides, no size difference can be highlighted in as-deposited materials according to the gold islands exhibited in either the A- or B-type orientation relationships. On the basis of those observations, we have no explanation concerning this peculiarity and we cannot ascribe it to the presence of oxygen vacancies. Nonetheless, as small metal supported nanoparticle morphology is soundly linked to the support surface modifications, this work proves that the interface structure is as well.

**Larger Gold Islands (>5 nm).** Similar experiments were performed for the Au/ $\text{CeO}_2$ -CP sample. This exhibits similar gold nanoparticles to those produced by deposition–precipitation, except for their size (>5 nm) and consequently their morphology.

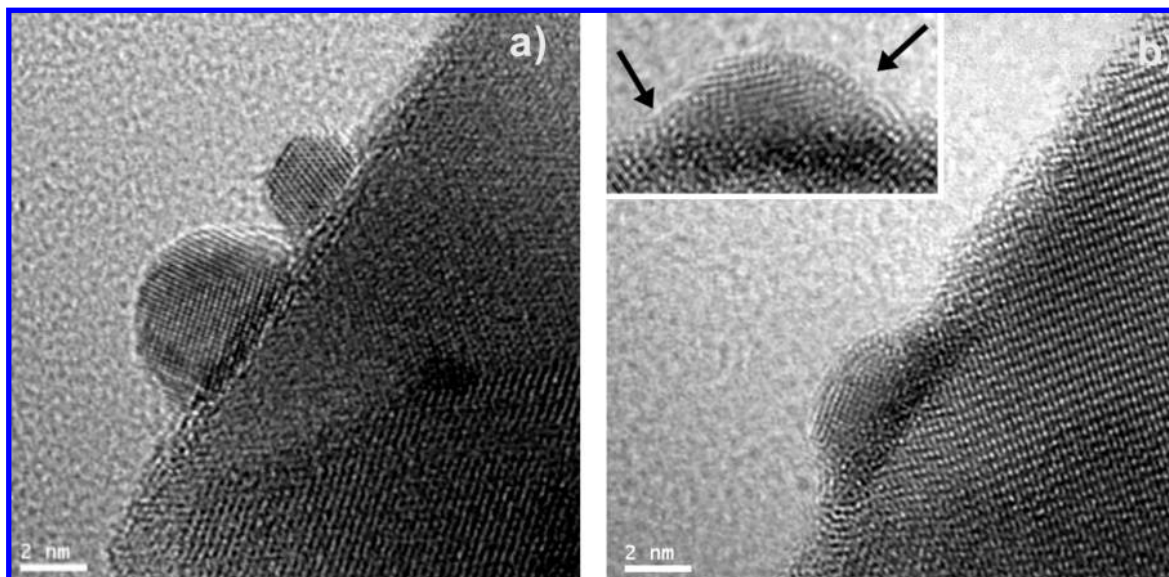


**Figure 6.** (a) HRTEM micrograph of as-deposited Au/CeO<sub>2</sub>-CP material. (b) HRTEM micrograph extracted from the video sequence illustrating the beginning of the encapsulation process of the bigger gold island by a CeO<sub>2-x</sub> layer (pointed by arrows), while the smallest one has already disappeared.

Before the electron beam was focused, Figure 5a shows a 12 nm diameter gold island with an hemispherical morphology and with the presence of {111} surface small steps.

On the first stage of the electron beam illumination, diffusion of gold atoms occurs. Some {111} terraces are formed and the gold island is flattened: the contact angle between gold and ceria decreases. The video sequence ends while the morphology of the island has notably changed. No more terraces are visible and a contrast perturbation has occurred at the interface between gold and ceria. A thin layer, not yet organized, covering the gold particle starting from its left upper hand side appears. Figure 5c has been captured only a few minutes after the end of the video sequence while the electron beam is still focused on the Au/CeO<sub>2</sub> interface. The layer covering the gold island is crystallized. The reticular distance is {022}<sub>CeO<sub>2</sub></sub>. Moreover, this layer is bending to perfectly fit the gold island surface curvature. The gold lattice plane contrast has also disappeared and is now blurred by the one of the underlying oxide: the whole supported gold particle is encapsulated. At the last observation stage (Figure 5d), the encapsulating layer is still organized and exhibits a zone axis on the left upper hand side of the gold island.

In contrast to Au/CeO<sub>2</sub>-DP sample, the diffusion of gold atoms is reduced for Au/CeO<sub>2</sub>-CP. Only surface reorganization of gold particles is detected. This difference between both samples is attributed to size difference and not to the chemical difference of the substrate resulting from the conditions of preparation. The melting temperature of gold particles of 12 nm diameter is comparable to the bulk gold.<sup>63</sup> In addition, the large particles exhibit small surface tension and large adhesion energy with the substrate. These different factors limit the atomic gold diffusion. The size effect will be confirmed below with additional experiments which have been performed on samples containing both small and large gold particles on ceria surface.

Encapsulation of the gold island is highlighted. Such decoration of supported metal nanoparticles has already been observed and takes part in the so-called strong metal–support interaction (SMSI).<sup>40,41,43,66–70</sup> These SMSI are considered to significantly affect the microstructure and properties of catalysts. Liotta et al. summarized the explanations that have been given for the influence of oxidative/reductive treatments on the activity of

the Pt catalyst supported on CeO<sub>2</sub> or CeO<sub>2</sub>–ZrO<sub>2</sub>: (i) alloy formation between Pt and Ce; (ii) decoration or encapsulation of Pt by partially reduced ceria (500 °C <  $T_{red}$  < 900 °C); and (iii) pure electronic interactions.<sup>71</sup> To encapsulate supported metal particles, cerium species are thought to migrate during the reductive treatment from the bulk to the surface of the support, resulting in the formation of ceria-rich phase on the surface. The migration of a reduced support layer to the top of the metal crystallite, rather than the burial of this layer into the bulk, is the most likely decoration mechanism. This process is noteworthy for the catalytic activity since encapsulated particles are inaccessible to gas-phase molecules and cannot thus participate on catalysis.

For the studied Au/CeO<sub>2</sub> system, there is a possibility that the Au/CeO<sub>2</sub> interface becomes Ce-rich under the present irradiation conditions. There should occur the Au–Ce alloy formation at or near the interface due to the presence of the Au–Ce alloy phase with low melting point in the phase diagram, as suggested by Akita.<sup>43</sup> This could explain the contrast perturbation observed near the Au/CeO<sub>2</sub> interface region in both Figure 5b and the video sequence.

Mobility of the cerium atoms is then allowed by the creation of oxygen vacancies. In Figure 5b, they start to decorate the gold island, which is finally encapsulated by a 2 nm thick CeO<sub>2</sub> layer (Figure 5c). Thanks to the measurement of the {022}<sub>CeO<sub>2</sub></sub> reticular distance, we give here the experimental proof that nonreduced cerium species are the constituents of the first encapsulating layer.

During the decoration process, the gold particle surface is no more formed by steps or terraces. We cannot identify the structural nature of the interface plane between the gold nanoparticle and the encapsulating layer, but we can reasonably think that {022}<sub>CeO<sub>2</sub></sub> planes and {002}<sub>Au</sub> ones are facing each other (Figures 5, a and c). The interface mismatch is only about 6.6%. Contrary to the 25% mismatch observed earlier, the 6.6%’s one can be matched elastically. When gold, the softer material, is deposited on ceria, the system favors a compact {111} interface plane to the detriment of the lattice mismatch which is compensated by the creation of a dislocation network into the gold nanoparticle. On the contrary, when ceria is



encapsulating a gold island and then forming a CeO<sub>2</sub>/Au interface, the system tends to minimize the lattice misfit.

The last stage of this encapsulation process is the reduction of the CeO<sub>2</sub> layer. Akita et al. performed electron energy loss spectroscopy (EELS) experiments on a gold nanoparticle decorated by a cerium-rich layer.<sup>43</sup> They pointed out that this surface layer is not Ce<sup>4+</sup> but Ce<sup>3+</sup> or a mixture of both, which can correspond to several CeO<sub>2-x</sub> compounds with  $x$  varying from 1/6 to 1. The geometry of the zone axis presented in Figure 5d coupled with the reticular distances measured discards crystallographic structures other than cubic ones. Only five cubic structures belonging to  $Fm\bar{3}m$  and  $Ia\bar{3}$  space groups and with  $0.305 < x < 1$  remain. From measurements on HRTEM images, we are able to propose a lattice parameter for both  $Fm\bar{3}m$  and  $Ia\bar{3}$  hypothesis:  $5.7 \text{ \AA} < a < 5.8 \text{ \AA}$  and  $11.4 \text{ \AA} < a < 11.6 \text{ \AA}$ , respectively. Strictly speaking, this lattice parameter could only correspond to the  $Ia\bar{3}$  Ce<sub>2</sub>O<sub>3</sub> structure ( $a = 11.41 \text{ \AA}$ ) issued from ab initio calculations (ICDS #96202). However, taking into account strong local lattice distortions due to the bending of the encapsulating layer, we can consider that this could also be identified as the  $Fm\bar{3}m$  CeO<sub>1.66</sub> structure (ICDS #88757). Further experiments need to be carried out to fully determine the crystallographic nature of this encapsulating layer.

In order to outline the size effect and demonstrate that the different processes observed above are independent of the surface chemistry effects of the substrate used for supporting the gold nanoparticles, an experiment was carried out on a Au/CeO<sub>2</sub>-CP sample where a small and a large deposited gold islands coexist on ceria subsurface (Figure 6). At the beginning of the electron beam illumination, the smallest gold island shrinks layer by layer until its complete disappearance. A few seconds later, the large gold particle becomes flattened but remains on its CeO<sub>2</sub> support. The contrast at the interface between Au and CeO<sub>2</sub> becomes distorted indicating the Au–Ce alloy formation. The encapsulation process then proceeds leading to a gold cluster covered up by a CeO<sub>2-x</sub> layer. This experiment clearly illustrates the size effect on the stability of gold particles onto ceria subsurface.

#### 4. Conclusions

The structural stability of the gold nanoparticles under electron beam-induced heating and reduction has been investigated. The results of the experiments show that the stability of gold islands on ceria support is strongly dependent on the metal particle size.

(i) Small-sized gold islands (<5 nm) shrink layer by layer under focused electron beam. The driving forces of the observed shrinkage are the local temperature rise and the creation of oxygen vacancies on the ceria. Spreading the electron beam leads to a return of the gold atoms to their initial location. Despite a few morphology and interfacial structure changes, the process is entirely reversible. This appearance–disappearance process can have an impact on the catalytic power of the Au/CeO<sub>2</sub> materials since gold nanoparticles larger than 5 nm are not active for the CO oxidation.<sup>28</sup>

(ii) Larger gold particles become encapsulated by a cerium-rich thin layer. Experimental proofs of the four-step encapsulation process are shown. (1) Increase of the adhesion energy between gold and ceria and contact angle decrease promoted by the creation of oxygen defects. (2) Formation of an Au–Ce alloy phase in the interface region. (3) Decoration of gold nanostructure by a CeO<sub>2</sub> thin layer in such a way to favor a relatively low lattice mismatch at the interface. (4) Reduction of the ceria layer into a CeO<sub>2-x</sub> layer.

**Acknowledgment.** The authors thank the CREMEM-University of Bordeaux for its electron microscopy facilities and A. Demourgues for fruitful discussions.

#### References and Notes

- (1) Faraday, M. *Philos. Trans. R. Soc. London* **1834**, 124, 77.
- (2) Hammer, B.; Norskov, J. K. *Nature (London)* **1995**, 376, 232.
- (3) Bond, G. C.; Sermon, P. A. *Gold Bull.* **1973**, 6, 102.
- (4) Haruta, M.; Kobayashi, T.; Sano, H.; Yamada, N. *Chem. Lett.* **1987**, 2, 405.
- (5) Haruta, M.; Yamada, N.; Kobayashi, T.; Iijima, S. *J. Catal.* **1989**, 115, 301.
- (6) Hutchings, G. J. *J. Catal.* **1985**, 69, 292.
- (7) Haruta, M. *Catal. Today* **1997**, 36, 15.
- (8) Valden, M.; Lai, X.; Goodman, D. W. *Science* **1998**, 281, 1647.
- (9) Haruta, M.; Tsubota, S.; Kobayashi, T.; Kageyama, H.; Genet, M. J.; Delmon, B. *J. Catal.* **1993**, 144, 175.
- (10) Kobayashi, T. *Sens. Actuators B* **1990**, 1, 222.
- (11) Okumura, M.; Tsubota, S.; Iwamoto, M.; Haruta, M. *Chem. Lett.* **1998**, 315.
- (12) Yuan, Y.; Kozlova, A. P.; Asakura, K.; Wan, H.; Tsai, K.; Iwasawa, Y. *J. Catal.* **1997**, 170, 191.
- (13) Grunwaldt, J. D.; Kiener, C.; Wögerbauer, C.; Baiker, A. *J. Catal.* **1999**, 181, 223.
- (14) Zanella, R.; Giorgio, S.; Shin, C. H.; Henry, C. R.; Louis, C. J. *Catal.* **2004**, 222, 357.
- (15) Lin, S. D.; Bollinger, M.; Vannice, M. A. *Catal. Lett.* **1993**, 17, 245.
- (16) Grunwaldt, J. D.; Maciejewski, M.; Becker, O. S.; Fabrizioli, P.; Baiker, A. *J. Catal.* **1999**, 186, 458.
- (17) Grunwaldt, J. D.; Baiker, A. *J. Phys. Chem. B* **1999**, 103, 1002.
- (18) Bamwenda, G. R.; Tsubota, S.; Nakamura, T.; Haruta, M. *Catal. Lett.* **1997**, 44, 83.
- (19) Okumura, M.; Tanaka, K.; Ueda, A.; Haruta, M. *Solid State Ionics* **1997**, 95, 143.
- (20) Costello, C. K.; Kung, M. C.; Oh, H. S.; Kung, K. H. *Appl. Catal., A* **2002**, 232, 159.
- (21) Kung, H. H.; Kung, M. C.; Costello, C. K. *J. Catal.* **2003**, 216, 425.
- (22) Boccuzzi, F.; Chiorino, A.; Manzoli, M.; Andreeva, D.; Tabakova, T. *J. Catal.* **1999**, 188, 176.
- (23) Carrettin, S.; Concepcion, P.; Corma, A.; Lopez-Nieto, J. M.; Puentes, V. F. *Angew. Chem., Int. Ed.* **2004**, 43, 2538.
- (24) Moreau, F.; Bond, G. C. *Catal. Today* **2006**, 114, 362.
- (25) Guzman, J.; Carrettin, S.; Corma, A. *J. Am. Chem. Soc.* **2005**, 127, 3286.
- (26) Okumura, M.; Nakamura, S.; Tsubota, S.; Nakamura, T.; Azuma, M.; Haruta, M. *Catal. Lett.* **1998**, 51, 53.
- (27) Venezia, A. M.; Liotta, L. F.; Pantaleo, G.; Parola, V. L.; Deganello, G.; Beck, A.; Koppány, Z.; Frey, K.; Horvath, D.; Gucci, L. *Appl. Catal., A* **2003**, 251, 359.
- (28) Bond, G. C.; Thompson, D. T. *Gold Bull.* **2000**, 33 (2), 41.
- (29) Bond, G. C.; Thompson, D. T. *Catal. Rev.—Sci. Eng.* **1999**, 41, 319.
- (30) Schubert, M. M.; Hackenberg, S.; Van Veen, A. C.; Muhler, M.; Plzak, V.; Behm, R. J. *J. Catal.* **2001**, 197, 113.
- (31) Liu, H.; Kozlov, A. I.; Kozlova, A. P.; Shido, T.; Asakura, K.; Iwasawa, Y. *J. Catal.* **1999**, 185, 252.
- (32) Frost, J. C. *Nature (London)* **1988**, 18, 577.
- (33) Trovarelli, A. *Catal. Rev.—Sci. Eng.* **1996**, 38, 439.
- (34) Rao, G. R.; Kaspar, J.; Di Monte, R.; Meriani, S.; Graziani, M. *Catal. Lett.* **1994**, 24, 107.
- (35) Trovarelli, A.; Dolcetti, G.; de Leitenburg, C.; Kaspar, J.; Finetti, P.; Santoni, A. *J. Chem. Soc., Faraday Trans.* **1992**, 88, 1311.
- (36) Serre, C.; Garin, F.; Belot, G.; Maire, G. *J. Catal.* **1993**, 141, 9.
- (37) Fu, Q.; Saltsburg, H.; Flytzani-Stephanopoulos, M. *Science* **2003**, 301, 935.
- (38) Venezia, A. M.; Pantaleo, G.; Longo, A.; Di Carlo, G.; Casaleto, M. P.; Liotta, L.; Deganello, G. *J. Phys. Chem. B* **2005**, 109, 2821.
- (39) Kang, Y. M.; Wan, B. Z. *Catal. Today* **1999**, 26, 59.
- (40) Bernal, S.; Botana, F. J.; Calvino, J. J.; Cifredo, G. A.; Pérez-Omil, J. A.; Pintado, J. M. *Catal. Today* **1995**, 23, 219.
- (41) Bernal, S.; Calvino, J. J.; Cauqui, M. A.; Gatica, J. M.; Larese, C.; Pérez-Omil, J. A.; Pintado, J. M. *Catal. Today* **1999**, 50, 175.
- (42) Akita, T.; Okumura, M.; Tanaka, K.; Kohyama, M.; Haruta, M. *J. Mater. Sci.* **2005**, 40, 3101.
- (43) Akita, T.; Okumura, M.; Tanaka, K.; Kohyama, M.; Haruta, M. *Catal. Today* **2006**, 117, 62.
- (44) Akita, T.; Tanaka, K.; Kohyama, M.; Haruta, M. *Catal. Today* **2007**, 122, 233.

- (45) Tauster, S. J.; Fung, S. C.; Garten, R. L. *J. Am. Chem. Soc.* **1978**, *100*, 170.
- (46) Tauster, S. J.; Fung, S. C. *J. Catal.* **1978**, *55*, 29.
- (47) Meriaudeau, P.; Dutel, J. F.; Dufaux, M.; Naccache, C. *Stud. Surf. Sci. Catal.* **1982**, *11*, 95.
- (48) Meriaudeau, P.; Dutel, J. F.; Dufaux, M.; Naccache, C. *Strong Metal Support Interactions, ACS Symp. Ser.* **1986**, 298, 118.
- (49) Bensalem, A.; Muller, J. C.; Tessier, D.; Bozon-Verduraz, F. *J. Chem. Soc., Faraday Trans.* **1996**, *92*, 3233.
- (50) Barrault, J.; Alouche, A.; Paul-Boncour, V.; Hilaire, L.; Percheron-Guegan, A. *Appl. Catal.* **1989**, *46*, 269.
- (51) Bernal, S.; Botana, F. J.; Calvino, J. J.; Cauqui, M. A.; Cifredo, G. A.; Jobacho, A.; Pintado, J. M.; Rodriguez-Izquierdo, J. M. *J. Phys. Chem.* **1993**, *97*, 4118.
- (52) Bernal, S.; Blanco, G.; Calvino, J. J.; Lopez-Cartes, C.; Perez-Omil, J. A.; Gatica, J. M.; Stephan, O.; Colliex, C. *Catal. Lett.* **2001**, *76* (3–4), 131.
- (53) Garvie, L. A. J.; Buseck, P. R. *J. Phys. Chem. Solids* **1999**, *60*, 1943.
- (54) Berger, S. D.; Macaulay, J. M.; Brown, L. M. *Philos. Mag. Lett.* **1987**, *56*, 179.
- (55) Takeguchi, M.; Tanaka, M.; Furuya, K. *Appl. Surf. Sci.* **1999**, *146*, 257.
- (56) Smith, D. J.; Bursill, L. A. *Ultramicroscopy* **1985**, *17*, 387.
- (57) Buckett, M. I.; Strane, J.; Luzzi, D. E.; Zhang, J. P.; Wessels, B. W.; Marks, L. D. *Ultramicroscopy* **1989**, *29*, 217.
- (58) Sayle, D. C.; Feng, X.; Ding, Y.; Wang, Z. L.; Sayle, T. X. T. *J. Am. Chem. Soc.* **2007**, *129*, 7924.
- (59) Sayle, T. X. T.; Parker, S. C.; Catlow, C. R. A. *Surf. Sci.* **1994**, *316*, 329.
- (60) Majimel, J.; Baccinello, D.; Durand, E.; Tréguer-Delapierre, M. *Langmuir* **2008**, *24*, 4289.
- (61) Goniakowski, J.; Mottet, C.; Noguera, C. *Phys. Status Solidi B* **2006**, *243* (11), 2516.
- (62) Henry, C. R. *Prog. Surf. Sci.* **2005**, *80*, 92.
- (63) Buffat, P.; Borel, J. P. *Phys. Rev. A* **1976**, *13*, 2287.
- (64) Tréguer-Delapierre, M.; Majimel, J.; Mornet, S.; Duguet, E.; Ravaine, S. *Gold Bull.* **2008**, *41* (2), 195.
- (65) Okazaki, K.; Morikawa, Y.; Tanaka, S.; Tanaka, K.; Kohyama, M. *Phys. Rev. B* **2004**, *69*, 235404.
- (66) Graham, G. W.; Jen, H. W.; Chun, W.; McCabe, R. W. *J. Catal.* **1999**, *182*, 228.
- (67) Stakheev, A. Y.; Kustov, L. M. *Appl. Catal. A* **1999**, *188*, 3.
- (68) Yeung, C. M. Y.; Yu, K. M. K.; Fu, Q. J.; Thompson, D.; Petch, M. I.; Tsang, S. C. *J. Am. Chem. Soc.* **2005**, *127*, 18010.
- (69) Fan, J.; Wu, X.; Ran, R.; Weng, D. *Appl. Surf. Sci.* **2005**, *245*, 162.
- (70) Fan, J.; Wu, X.; Yang, L.; Weng, D. *Catal. Today* **2007**, *126*, 303.
- (71) Liotta, L. F.; Longo, A.; Macaluso, A.; Martorana, A.; Pantaleo, G.; Venezia, A. M.; Deganello, G. *Appl. Catal. B* **2004**, *48*, 133.

JP9001115